metals

Article

Research on the Influence of the Isothermal Normalizing Cooling Rate on the Mechanically Polished Surface Roughness of Wind Power Gear Blanks

Yuhao Wang [1], Aijun Deng [1], Guozhong Jin [1,2], Shengfu Wu [2], Song Ye [1] and Zhenyi Huang [1,*]

[1] School of Metallurgical Engineering, Anhui University of Technology, Ma'anshan 243032, China; wyh_02200012@163.com (Y.W.); ajdeng@ahut.edu.cn (A.D.); jinguozhong@163.com (G.J.); yesong20250409@163.com (S.Y.)
[2] Technical Center, Maanshan Iron and Steel Co., Ltd., Ma'anshan 243000, China; sfwu0910@126.com
* Correspondence: huangzhenyi@ahut.edu.cn

Abstract

This study takes 18CrNiMo7-6 wind power gear steel as the object. Following the first holding stage of isothermal normalizing, the 18CrNiMo7-6 wind power gear blanks were cooled to the isothermal temperature via air cooling (AC) and forced-air cooling (FA), respectively. The influence of cooling rate on the roughness of the mechanically polished surface of wind power gear blanks was comprehensively studied by means of white light interference, EBSD, TEM, DSC and other technical characterization methods. The results show that a difference in cooling rate leads to a variation in the morphology and distribution of Cr-rich carbides (mainly Cr_7C_3), which affects the roughness of the mechanically polished surface. During air cooling (slow cooling), atoms diffuse fully. Owing to the relatively low cooling rate in the inner ring of the blank, C and Cr segregate, and abundant Cr-rich carbides precipitated and accumulated at grain boundaries, forming coarse blocky structures. This resulted in uneven mechanically polished surfaces and bright spot defects. The average roughness of the inner and outer ring is 2.648 nm and 2.096 nm, respectively. Forced-air cooling (fast cooling) eliminates surface quality defects by inhibiting long-range atomic diffusion. Meanwhile, radial elemental segregation in the original cast blanks was inherited in subsequent processes, which affected the uniformity of carbide precipitation during cooling. In addition, the differences in cooling rates will also cause variations in the precipitation temperatures of carbides in steel, which in turn further affects the homogenization distribution of carbides in steel. This research provides a theoretical basis and an optimization method for the microstructural regulation and surface quality enhancement of wind power gear steel.

Keywords: 18CrNiMo7-6 steel; heat treatment; cooling rate; surface topography; carbides

Check for updates

Academic Editor: Bernd-Arno Behrens

Received: 26 January 2026
Revised: 15 February 2026
Accepted: 18 February 2026
Published: 28 February 2026

Copyright: © 2026 by the authors. Licensee MDPI, Basel, Switzerland. This article is an open access article distributed under the terms and conditions of the Creative Commons Attribution (CC BY) license.

1. Introduction

18CrNiMo7-6 gear steel is a key material widely used in advanced equipment in the aerospace, wind power generation and automotive industries, and its performance is critical to the service life and reliability of components [1,2]. The core performance requirements for gear steel include high contact fatigue strength, bending fatigue strength, and a well-matched combination of core toughness and surface hardness [3,4]. For wind power applications, 18CrNiMo7-6 steel requires high strength to withstand heavy load impacts, high hardenability to ensure structural uniformity, high toughness to resist load

impacts, excellent fatigue performance to avoid long-term operational failure, and good machinability to ensure the precision of finished products. Its processing performance, comprehensive mechanical properties and fatigue properties directly determine the operating reliability and service life of the transmission system, and forging–tooth–carburizing and other core process controls are the focus of gear steel preparation. Both forging–gear-forming–carburizing and heat treatment processes have an effect on the fatigue properties of the finished product, with heat treatment being the key to the fatigue properties of the gear blank. For 18CrNiMo7-6 steel subjected to multi-step heat treatments (normalizing, annealing, hardening, sub-zero quenching and tempering), it was found that heat treatments combined with machining, hot forging and cold spinning could improve the hardness, tensile properties and fatigue performance [5]. Due to the existence of initial stress distributions after the forging heat treatment, the cutting process and the formation of teeth will cause some impact. A study shows that the gear is subject to tensile stress inside the surface of the compressive stress and the top of the tooth region of the smallest residual stress, which is the root region of the tooth maximum [6]. Residual stress can lead to significant deterioration in contact fatigue performance, which can still have a serious impact on fatigue performance after plastic reloading has occurred [7]. The surface inhomogeneity induced by machining further degrades the quality of finished products; when surface roughness is considered, the near-surface region is subject to both fatigue damage and extensive ratchet damage with increasing load [8,9].

Surface roughness is critical to the fatigue performance of gear steels, and in general, the fatigue life of engineered components increases as surface roughness decreases [10–12]. Scanning electron beam pretreatment (SEBP) of 22CrMoH gear steel found that SEBP promotes the adsorption of carbon atoms on the surface in the gas carburizing process by increasing the surface roughness, improves the efficiency of gas carburizing, and makes the grain refining effect more obvious while reducing the friction coefficient [13]. In a study of AISI 9310 gear steel, it was found that the strategy of using a shot peening process prior to carburizing also increased the surface roughness and improved the effective hardening depth and surface hardness of the carburized steel [14]. In addition, in carburizing pretreatment, process strategies such as laser impact shot peening [15], plasma nitriding [16], and ultrasonic rolling [17] were used, and all of them obtained the conclusion that increasing surface roughness has a positive effect on the enhancement of the effective hardening depth (EHD) after carburizing or nitriding heat treatment. Nitriding experiments on 304 SS after Surface Mechanical Abrasion Treatment (SMAT) showed that the detrimental effect, if any, of increased surface roughness on nitriding was superseded by the favorable effect of martensite in promoting nitrogen diffusion, and that SMAT-treated Cr was more readily migrated [18]. A composite heat treatment technique based on vacuum carburizing and ion nitriding for the low carbon alloy steel 17CrNiMo6 found that the supersonic fine particle bombardment (SFPB) pretreatment + vacuum carburizing + rare earth lanthanum + examples of nitriding samples: S(La)-C-PN, showed superior wear and corrosion resistance properties [19]. For laser surface melted gear steels, the strong shot peening process (LSMSSP) is superior in fatigue performance even though the surface roughness is higher than conventional shot peening (LSMTSP) [20]. Some studies have also suggested that the impairment of fatigue life is not due to surface roughness, but is influenced by coarse particles in the forged surface [21]. The influence of roughness on fatigue life does not meet expectations. In high-cycle fatigue performance tests, an increase in roughness will shorten the fatigue life, but the low-cycle fatigue strength will increase [22].

Gear formation accuracy plays an important role in the surface roughness of the workpiece, and therefore also has a serious impact on the carburizing quality and fatigue life of gear steels. By strictly controlling the feed rate and rolling frequency of ultrasonic

rolling after forging, the surface roughness can be significantly reduced to improve surface integrity, and the stability and accuracy of subsequent gear forming processing can be enhanced [23], or improving the traditional grinding process can optimize the surface integrity and fatigue performance of the processed sample [24]. Due to problems such as uneven element distribution and severe segregation in 18CrNiMo7-6 gear steel [25], in the research on the influence of isothermal normalizing on the surface quality of mechanically polished processing and subsequent fatigue performance, the results show that the normalizing temperature has an impact on the grain size and uniformity of carburized gear steel. The ferrite grains formed at a lower normalizing temperature will transform into larger austenite grains, and the grain growth is closely related to the formation of carbonitride particles during the carburizing process [26]. The coarse structure that occurs after carburizing, quenching and tempering processes of gear steel is effectively controlled by controlling the forging temperature, adding an isothermal normalizing process and carburizing temperature, which effectively controls the coarse structure after carburizing, quenching and tempering [27].

Currently, relatively few studies have focused on carbide precipitation during isothermal normalizing in the tooth-forming stage of gear steel, particularly the effect of cooling rate on the uneven precipitation of carbides induced by elemental segregation in steel, which in turn leads to the sensitivity of cutting-induced surface roughness to cooling rate. This study takes 18CrNiMo7-6 as the object and adopts the isothermal normalizing process to systematically study the sensitivity of the cooling rate of the mechanically polished surface roughness and its influencing mechanism, providing an optimization idea for the microstructure control and mechanical property regulation of wind power gear steel.

2. Materials and Methods

2.1. Sample Preparation

The 18CrNiMo7-6 wind power gear steel used in this study was smelted and cast via electric arc furnace (EAF) + ladle furnace (LF) + vacuum degassing furnace (RH) + continuous casting (CC). The chemical composition is shown in Table 1. The size of the cast blank is Φ 500 mm × 883 mm. The forging process was conducted via free forging (triple upsetting and triple drawing), with a forging ratio of no less than 2 for each pass. The initial forging temperature is approximately 1190 °C, and the final forging temperature is greater than 850 °C. First, the gear steel was forged into a blank disk via the triple upsetting and triple drawing process, with a diameter close to the finished size. We used a 220–260 mm diameter punch, with the center of the forgings punching the formation of the inner ring, and then reaming the inner ring to the size of the finished product. The final forging for the outer ring had a diameter of 640 mm, the inner ring a diameter of 350 mm, and the forging material thickness was 480 mm of the disk.

Table 1. Chemical composition of 18CrNiMo7-6 (wt.%).

Test Steel	C	Si	Mn	P	S	Cr	Mo	Ni	Cu	Nb	Fe
18CrNiMo7-6	0.15~0.21	≤0.4	0.5~0.9	≤0.015	≤0.015	1.5~1.8	0.25~0.35	1.4~1.7	≤0.4	0.02	Bal.

2.2. Pilot Program

The forged samples were austenitized at 950 °C, then air-cooled (AC) to 690 °C and held at this temperature to complete austenite transformation, and finally air-cooled to room temperature. For the second batch of samples, the optimized process involved austenitization at 950 °C, followed by forced-air cooled (FA) to 690 °C, holding so that the

austenite transformation was completed, and then air-cooled to room temperature. The heat treatment program applied in this study is presented in Figure 1.

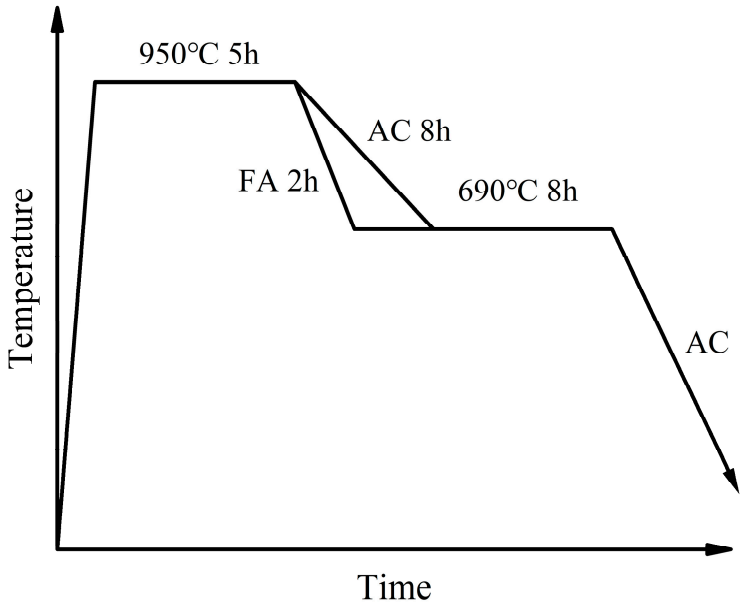


Figure 1. Heat treatment program.

2.3. Microstructural Characterization

Sampling was performed using a DK77-type electrical discharge wire cutting machine (Taizhou Ruite Machinery Equipment Co., Ltd., Taizhou, China) with the following parameters: cutting speed of 3 mm^2/min, feed rate of 1.5 mm/min, brass wire tool (Φ 0.18 mm), deionized water as the dielectric fluid, and cutting depth equal to the specimen thicknesses. All parameters were kept consistent for all samples to ensure machining uniformity, and white light interference tests were conducted to determine the roughness and three-dimensional morphology. Polishing was performed as follows: grinding with 240#, 800#, 1200# and 2000# SiC sandpapers, followed by polishing with 2.5 μm, 1.5 μm and 0.5 μm diamond pastes. The polishing disk rotation speed was 300 r/min with water cooling. Surface roughness was measured by a white light interferometer in non-contact mode, with a scanning area of 1.11 μm × 1.8 μm. The roughness parameter Ra was adopted for evaluation. Microhardness measurements were conducted using an HMV-2AD microhardness tester (Shimadzu (China) Co., Ltd., Shanghai, China), with microhardness values calculated by measuring the diagonal lengths of the indentations, and the specific experimental procedures are as follows: representative samples were cut along the diameter of the disc using a band sawing machine and the bulk sample was equally divided into 6 test areas along the diameter direction with a metallographic sample cutting machine, which were numbered 1# to 6# and arranged in sequence from the outer ring to the inner ring for separate testing. A TESCAN MIRA field-emission scanning electron microscope (SEM) (TESCAN, Brno, Czech Republic) was employed to conduct energy dispersive spectroscopy (EDS) for composition analysis, and electron probe micro-analysis (EPMA) was performed to characterize the element distribution in the experimental steel. Crystal Structure and Phase Distribution of Experimental Steel Analyzed by Electron Backscatter Diffraction Scanning Electron Microscopy (EBSD) Using JEOL JSM-7800FPRIME Model (JEOL Ltd., Tokyo, Japan). EBSD characterization was performed with a step size of 0.2 μm. The confidence index (CI) > 0.1 was used to ensure reliable indexing. Phase identification was conducted based on the distinct crystallographic structures and standard diffraction databases of ferrite, Cr_7C_3 and $Cr_{23}C_6$. Morphological observation and structural analysis

of the prepared thin zone samples and energy spectroscopy (EDS) analysis of the second phase particles were performed using a JEM-2100 transmission electron microscope (TEM) (JEOL Ltd., Tokyo, Japan). Differential Scanning Calorimetry (DSC) tests were carried out using a NETZSCH DSC 404F3 thermal analyzer (NETZSCH-Gerätebau GmbH, Selb, Germany) with a pure aluminum crucible, and the whole process was carried out under argon protection, with the temperature programmed from 1200 °C (full austenitization temperature) to 600 °C at cooling rates of 5 °C/min and 20 °C/min, respectively.

3. Results and Discussion

3.1. Macro Features

3.1.1. Macroscopic Characteristics of Machining

The macroscopic characteristics of the surface of the forging are shown in Figure 2. The inner ring surfaces of air-cooled samples exhibited streak-like bright spots visible to the naked eye, which were densely distributed on the inner and outer ring surfaces of the forged disks. Forced-air-cooled 18CrNiMo7-6 blank inner and outer rings do not show obvious surface quality defects, and the surface streak-like bright spot phenomenon disappeared.

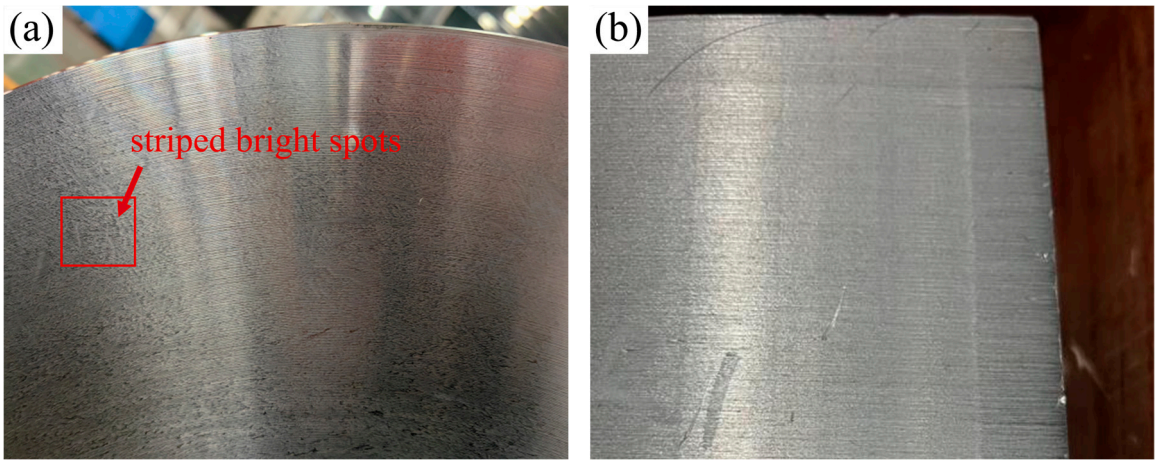


Figure 2. Macroscopic characteristics of bright spots of wind power gear blanks: (**a**) air-cooled; (**b**) forced-air-cooled.

3.1.2. White Light Interferometry Characteristics of the Polished Surface Contour

The roughness and three-dimensional profile of the polished surface were tested using a laser confocal microscope; before measurement, all specimens were mechanically polished to a mirror surface. The results are shown in Figure 3.

The results in Figure 2 show that after the wind power gear blank has been polished, the surface roughness of the air-cooled outer ring is lower than that of the inner ring. For statistical reliability, surface roughness measurements were performed at three different positions for each specimen; the average roughness values of the outer and inner rings were 2.096 ± 0.385 nm and 2.648 ± 0.054 nm, respectively. This result is consistent with the macroscopic morphological characteristics of the gear blank, that is, the inner ring presents more significant surface quality defects than the outer ring. The inner and outer rings of the gear blanks are relatively flat under the forced-air cooled process, with almost no difference in roughness.

Comparison of the results in Figures 3 and 4 shows that the air-cooled inner ring exhibits significant uneven morphology characteristics. This difference in surface morphology may be attributed to the inhomogeneous microhardness of the material's internal microstructure. During the cutting process, because the hard phase has stronger cutting resistance, the material cutting amount is relatively low and convex areas are formed, while

the soft phase forms concave areas because it is easier to cut, which ultimately leads to the formation of macroscopically visible surface quality defects on the surface. Forced-air-cooled gear blank inner and outer rings did not show significant uneven morphology features, and the inner and outer ring surface morphology differences are small. At this time the material internal organization of the micro-hardness is relatively uniform, so that the macroscopic visible surface quality defects disappear.

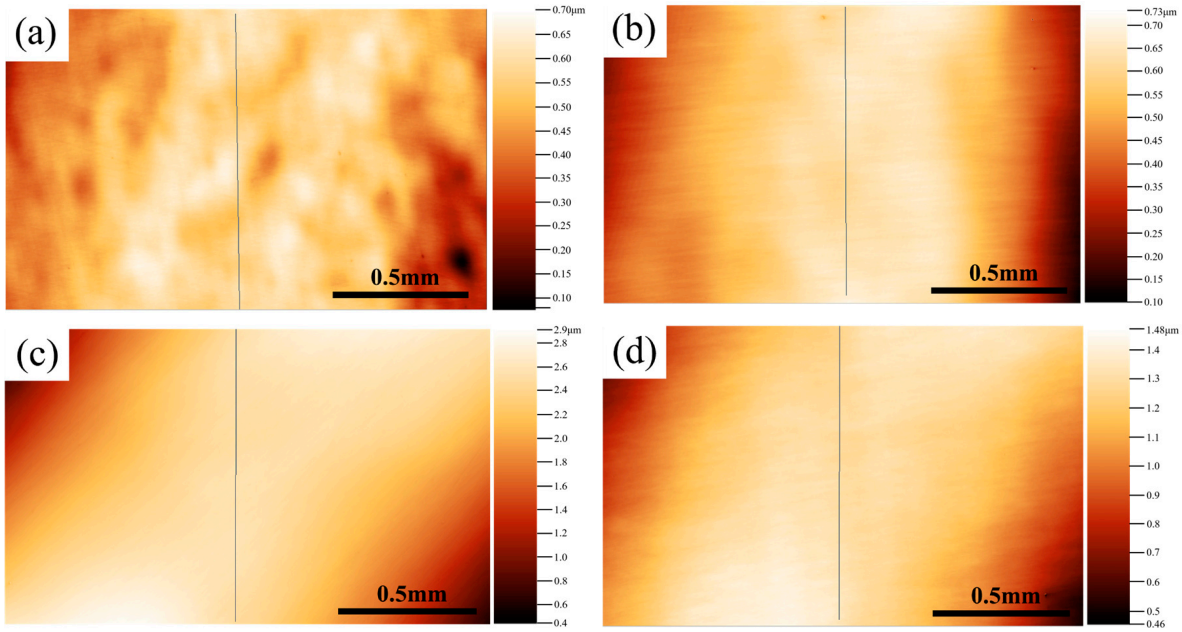


Figure 3. Roughness characteristics of the polished surface of wind power gear blanks: (**a**) air-cooled inner ring; (**b**) air-cooled outer ring; (**c**) forced-air-cooled Inner ring; (**d**) forced-air-cooled outer ring.

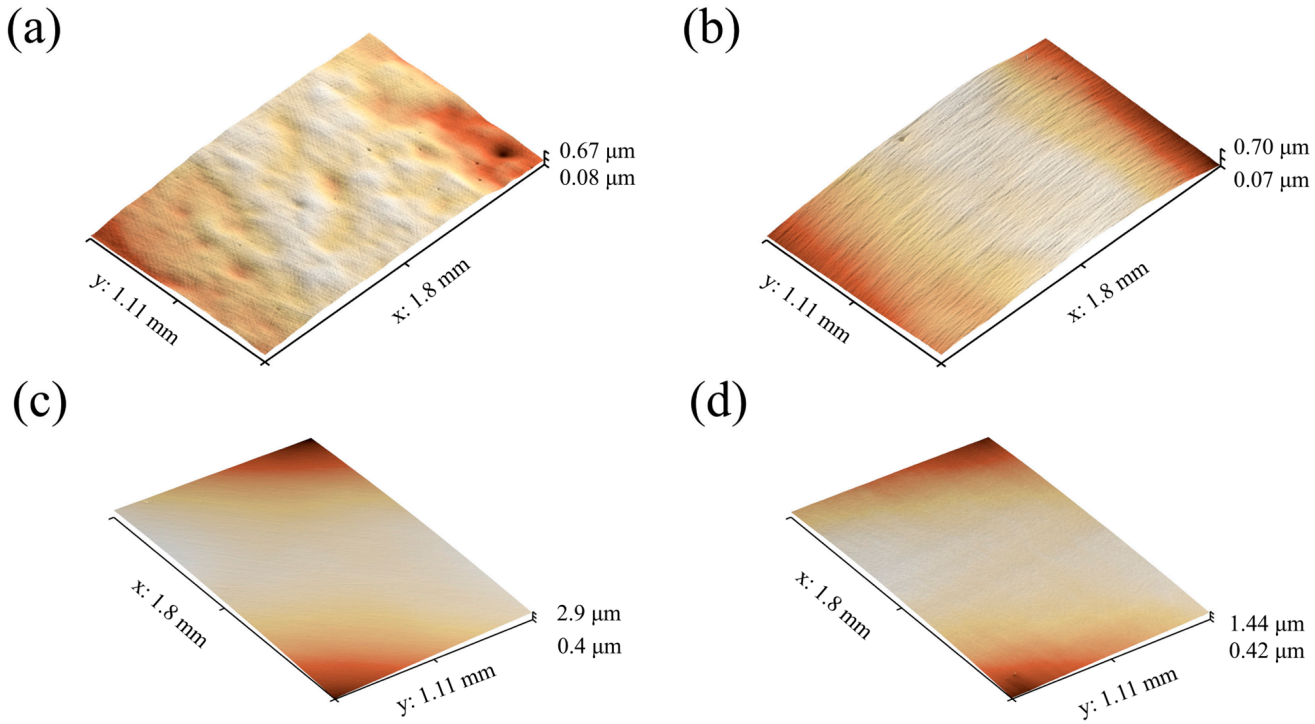


Figure 4. 3D profile characteristics of the polished surface of wind power gear blanks: (**a**) air-cooled inner ring; (**b**) air-cooled outer ring; (**c**) forced-air-cooled Inner ring; (**d**) forced-air-cooled outer ring.

3.1.3. Hardness Characteristics

In order to explore the formation mechanism of bright spots, the distribution characteristics of microhardness in the diameter direction of gear blanks were analyzed systematically. On each test area, a test matrix (9 × 6) is constructed vertical and parallel to the disk diameter direction, respectively. The intersection point of the matrix is the hardness test point. Multiple sets of metallographic photos are collected in each test area along the direction from the outer ring to the inner ring to ensure comprehensive and representative tissue characterization. The results are shown in Figure 5. The results of the hardness distribution cloud diagram show that the hardness of the air-cooled gear blank specimen with cutting bright spot characteristics has an obvious radial gradient distribution, and the hardness gradually decreases from the outer ring to the inner ring. From the perspective of phase transition dynamics, the cooling rate of the gear blank section changes in a gradient along the radial direction during the process of high-temperature austenitic air cooling to isothermal normalization temperature, that is, the cooling rate of the outer ring area is faster and the cooling rate of the inner ring area is slower. This difference in cooling rate leads to differences in the degree of supercooling between regions. The degree of supercooling in the outer ring area is larger. As the degree of supercooling decreases from the outer ring area to the inner ring area, the spacing between pearlite lamellae gradually increases [28], resulting in a decrease in material hardness. Furthermore, the pearlite transformation driving force decreases with the decrease in undercooling, which makes pearlite content decrease along radial direction and further reduces the hardness of the material.

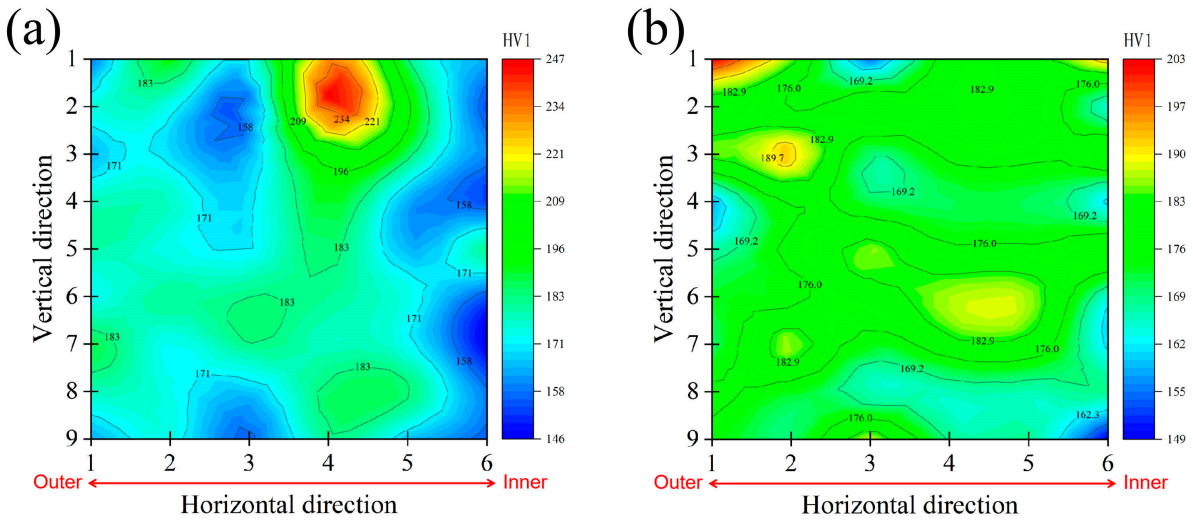


Figure 5. Hardness distribution cloud diagram of the wind power gear blank: (**a**) air-cooled; (**b**) forced-air-cooled.

3.2. Microscopic Features

3.2.1. Scanning Electron Microscope Organizational Characteristics

To investigate the typical SEM microstructural characteristics of wind power gear blanks from the outer to inner rings, EDS surface scanning was performed on the outer and inner ring regions, as well as their corresponding side regions. The test results are shown in Table 2.

From the quantitative elemental distribution data, the contents of the characteristic elements C, Cr and Si in air-cooled inner ring regions were significantly higher than those in outer ring regions, with the C element content difference being the most obvious. The contents of other alloying elements in the inner ring region are generally lower than those in the outer ring region. The forced-air-cooled specimens have significantly lower ele-

mental contents of Cr, Ni, Mo and Nb in the inner and outer rings, and the C content is much higher than that of the air-cooled group, which indicates that the cooling rate dominates the elemental content characteristics of the gear blank. This difference in composition may be related to the material's elemental segregation behavior during forging and heat treatment [29].

Table 2. EDS mapping composition results (wt.%) of typical regions in the inner-ring and outer-ring areas (wt.%).

Location	C	Si	Mn	Cr	Ni	Al	Nb
Air-cooled inner ring	86.00	7.07	3.32	1.46	0.79	0.00	0.42
Air-cooled outer ring	88.16	4.81	3.18	1.54	0.86	0.31	0.19
Air-cooled inner ring (side)	86.64	5.57	3.59	1.50	0.78	0.28	0.15
Air-cooled outer ring (side)	89.87	4.36	2.87	1.21	0.48	0.08	0.24
Forced-air-cooled inner ring	70.01	22.84	1.62	1.03	0.27	0.09	0.41
Forced-air-cooled outer ring	77.08	18.91	1.66	1.13	0.02	0.00	0.33

3.2.2. Electron Probe Microanalysis (EPMA)

To clarify the microstructure of the original blank of the gear blank, the composition analysis of the original cast blank without forging and heat treatment was carried out by the electron probe component.

By comparing Figure 6, it can be seen that the degree of segregation of Cr elements from the surface to the core shows obvious gradient changes. The surface area has a mild degree of segregation, the 1/4 diameter location has a moderate degree of segregation, and the 1/2 diameter shows the most severe segregation characteristics. This indicates that cast gear blanks are also affected by differences in cooling rates brought about by different positions, and that this characteristic is inherited at subsequent process stages, resulting in uneven tissue transformation and uneven distribution of machining deformation resistance during forging and heat treatment, which ultimately may be attributed to surface quality defects under isothermal normalizing process with air cooling rate.

To further explore the element distribution characteristics and analyze the element diffusion and precipitation behavior of the material, the EPMA surface scanning composition analysis was carried out on the inner ring area and outer ring area of the air-cooled gear blank. The results are shown in Figure 7.

The results in Figure 7 show that there are significant Cr, C and Mn segregation zones in the inner ring structure of air-cooled wind power gear steel, indicating that Cr-rich carbide phases may exist in this zone. Through comparative analysis, it is found that the density of the elemental segregation zone in the inner ring is significantly higher than that in the outer ring, which indicates that the number of Cr-rich carbides in the inner ring is significantly higher than that in the outer ring. Combined with Table 2, the increase in cooling rate will increase the content of Cr and the segregation density at the same time, which is completely consistent with the surface morphology characteristics observed after cutting of wind power gear blanks. The presence of significant Cr, C and Mn elemental segregation zones in the inner ring organization of the forced-air-cooled wind power gear steel suggests that significant Cr and C elemental segregation characteristics also exist in this region. Compared with the air-cooling process, it can be seen that the regions of forced-air-cooled gear blanks have lower density and more uniform distribution of elemental enrichment than air-cooled regions, which is consistent with the macroscopic characteristics of the forced-air-cooled gear blank samples. From the perspective of material processing performance, likely related to the microhardness of carbide being much higher than that of ferrite (F) and pearlite (P), the carbide-rich area during the cutting process shows stronger

cutting resistance, thus forming a bright area on the machining surface. On the other hand, the matrix area is relatively dark because of its weak cutting resistance, which finally leads to the macroscopic bright spot morphology of the mechanically polished surface, which may be attributed to the fact that the accumulation of Cr-rich carbides is the main reason for the quality defects of the mechanically polished surface.

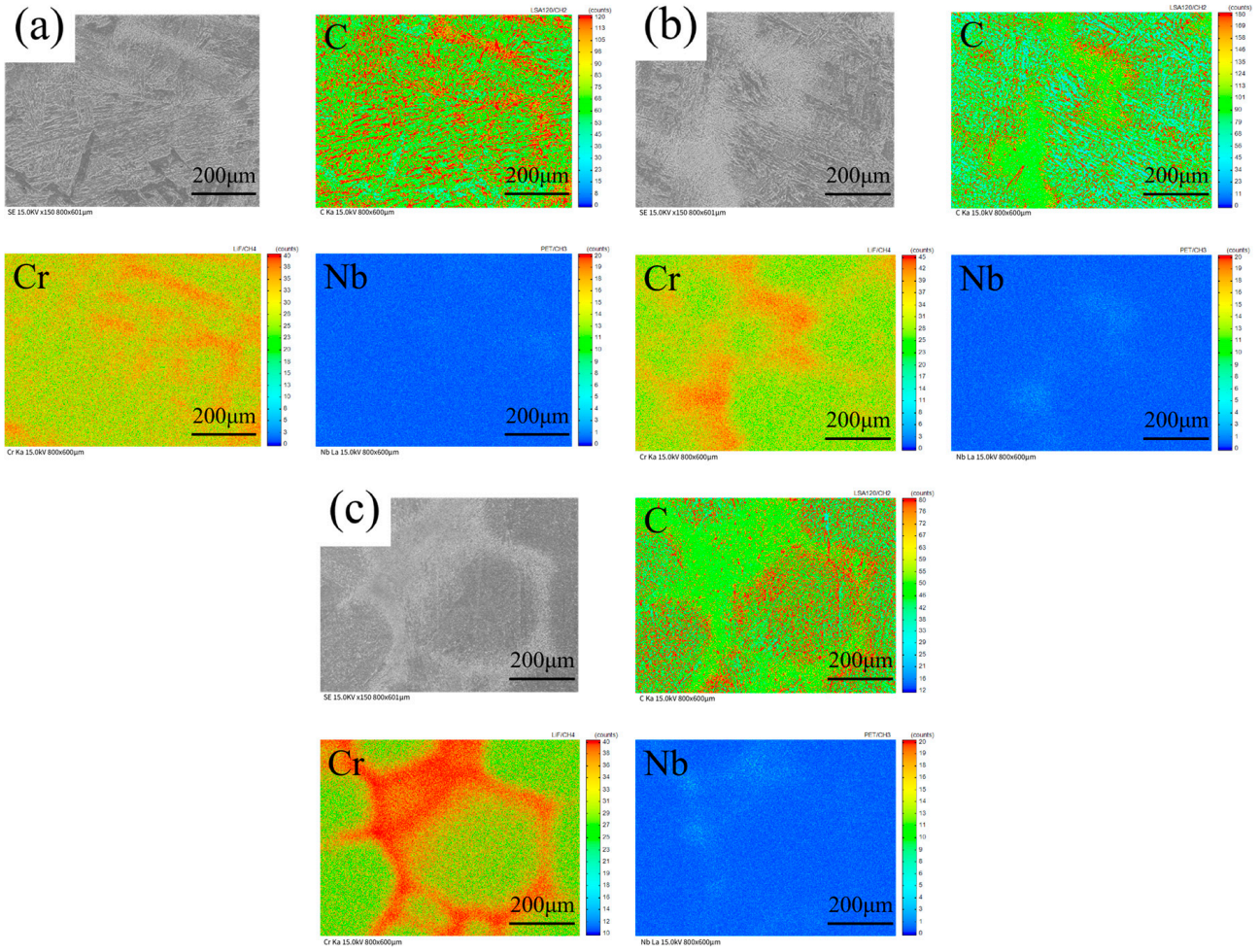


Figure 6. EPMA mapping analysis of the gear steel casting blank: (**a**) surface; (**b**) 1/4 diameter; (**c**) 1/2 diameter.

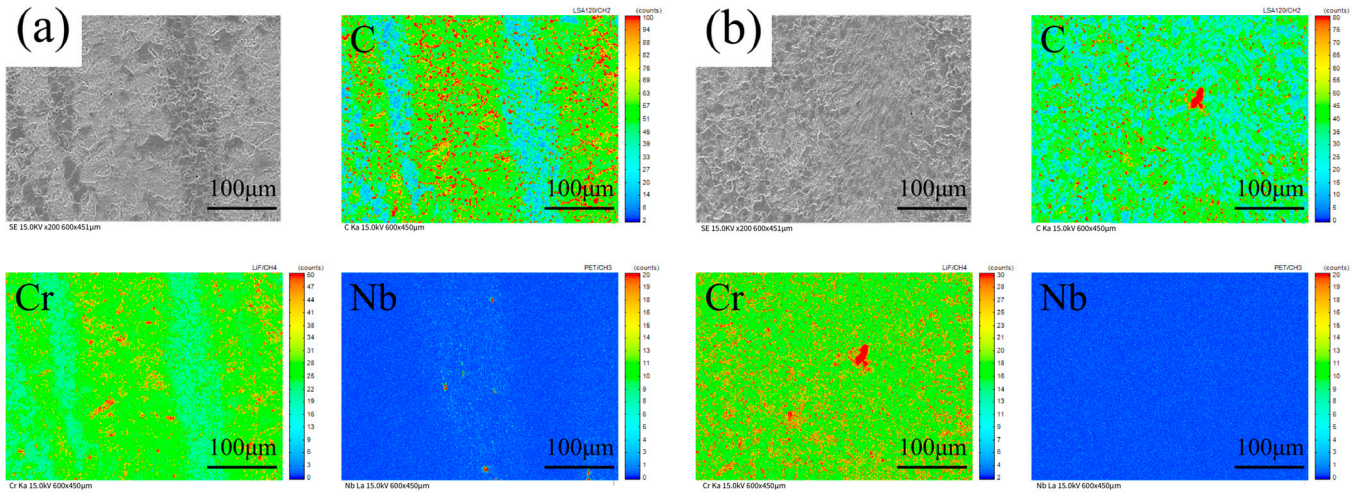


Figure 7. *Cont.*

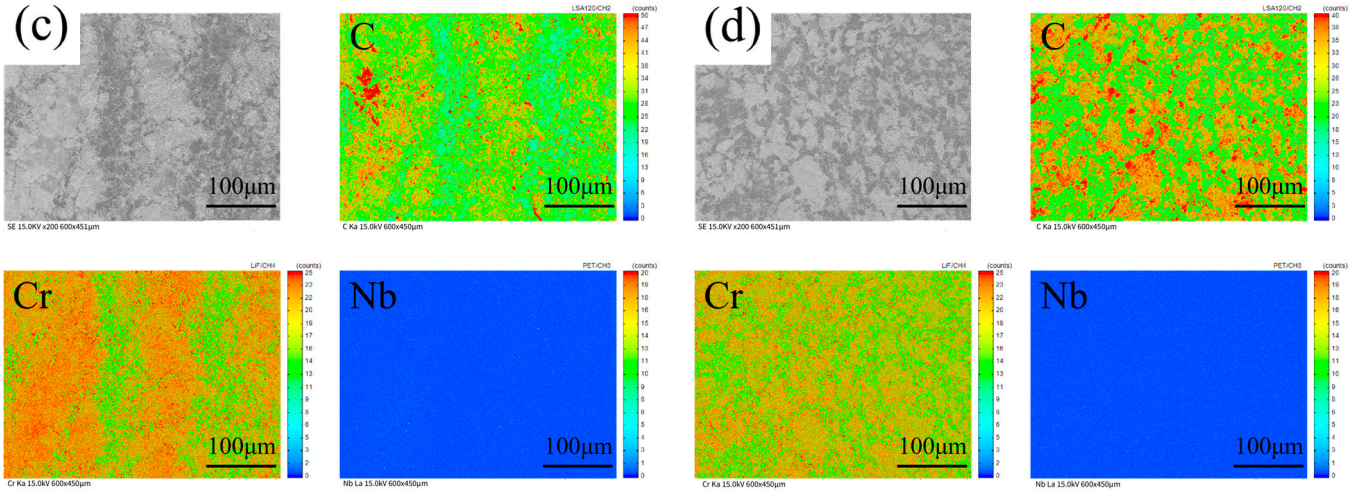


Figure 7. EPMA mapping analysis of wind power gear blank: (**a**) air-cooled inner ring; (**b**) air-cooled outer ring; (**c**) forced-air-cooled Inner ring; (**d**) forced-air-cooled outer ring.

3.2.3. Electron Backscatter Diffraction Analysis (EBSD)

To further investigate the characteristics of the physical phase relative composition of the carbide-enriched region of wind power gear blanks at different cooling speeds, electron backscattering diffraction (EBSD) was used to systematically analyze the physical phase of the inner and outer ring surfaces of the air-cooled specimens, and the results are shown in Figure 7.

The results of the EBSD phase distribution analysis show that there is a significant difference in the phase relative composition of the outer and inner rings of the air-cooled gear blanks. The microstructure of the outer ring consists mainly of ferrite (F), Cr_7C_3 carbides, carburite (Fe_3C) and NbC carbides, while the inner ring contains the same phases as the outer ring, in addition to a small relative amount of $Cr_{23}C_6$ carbides detected. Comparison of the carbide distribution characteristics between the air-cooled inner and outer rings reveals that the carbides in the inner ring region are mainly enriched at the grain boundaries, while the outer ring region exhibits a more uniform distribution. The forced-air-cooled gear blanks consisted of ferrite (F), Cr_7C_3 carbides, carburite (Fe_3C) and NbC carbides, none of which showed the $Cr_{23}C_6$ phase. The phase identification of Cr_7C_3 and $Cr_{23}C_6$ by EBSD was verified by combining their typical morphological and crystallographic characteristics reported in the published studies on 18CrNiMo7-6 steel, considering the limitation of EBSD alone in distinguishing these two carbides with similar lattice parameters [30,31]. Although $Cr_{23}C_6$ is the equilibrium carbide, the preferential precipitation of metastable Cr_7C_3 was observed under the non-equilibrium cooling conditions used in this study; this will be confirmed in thermodynamic calculations. Comparing the carbide distribution characteristics in each region of air-cooled and forced-air-cooled specimens, it can be observed that there is an overall more uniform carbide phase distribution under the forced-air-cooled cooling rate, which further illustrates that the cooling rate has a significant effect on the gear blank phase composition. In order to semi-quantitatively characterize the differences in Cr-containing carbides at different locations, the EBSD compositions were analyzed, as shown in Table 3.

It should be noted that the carbide fraction obtained by EBSD is semi-quantitative and relative, which is only used to reflect the precipitation trend, not an exact quantitative result. A comparative analysis revealed that the inner ring carbide semi-quantitative contents was significantly higher than the outer ring. Combined with Figure 8's air-cooled inner ring carbide distribution showing more obvious enrichment characteristics, and the results of the white light interference test (Figure 2), certain conclusions can be drawn. The slower cooling

rate of the inner ring will promote the precipitation of Cr-rich carbides, enriched carbide Cr_7C_3 by virtue of stronger cutting resistance, in the cutting process and the surrounding soft phase to form concave and convex morphological differences, ultimately leading to an increase in the roughness of the mechanically polished surface and the formation of macroscopic visible surface quality defects on the surface of the forging. The forced-air-cooled inner and outer ring Cr_7C_3 carbide semi-quantitative contents are both significantly lower than air-cooled specimens, while the inner ring carbide semi-quantitative contents are significantly higher than the outer ring in the same process. Combined with Figure 8, it can be judged that after increasing the cooling rate to the air-cooling rate, the precipitation of Cr-rich carbides is suppressed and shows a more uniform distribution, and the macroscopic surface quality defects are eliminated while obtaining a flat mechanically polished surface topography.

Table 3. EBSD relative composition results of the outer ring and inner ring (wt.%).

Location	F	Fe_3C	Cr_7C_3	NbC	$Cr_{23}C_6$
Air-cooled inner ring	98.8	0.06	0.75	0.02	0.002
Air-cooled outer ring	98.8	0.12	0.28	0.03	-
Forced-air-cooled inner ring	99.2	0.29	0.52	0.03	-
Forced-air -cooled outer ring	99.7	0.1	0.2	0.01	-

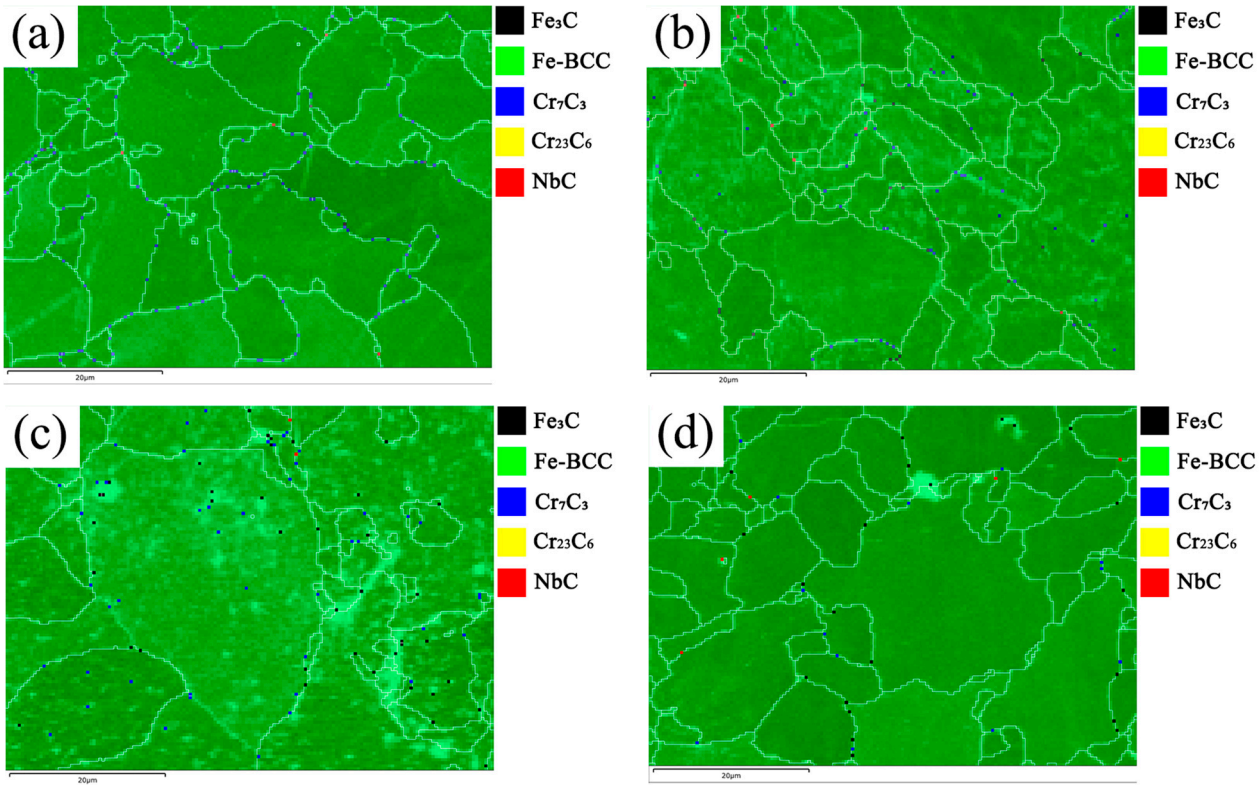


Figure 8. EBSD phase distribution results of the wind power gear blank: (**a**) air-cooled inner ring; (**b**) air-cooled outer ring; (**c**) forced-air-cooled inner ring; (**d**) forced-air-cooled outer ring.

3.2.4. Transmission Electron Microscopy Experimental Analysis (TEM)

In order to further characterize the microstructure and compositional distribution of the wind power gear blanks on the nanoscale, the material was experimentally analyzed by transmission electron microscopy, and the results are shown in Figure 9.

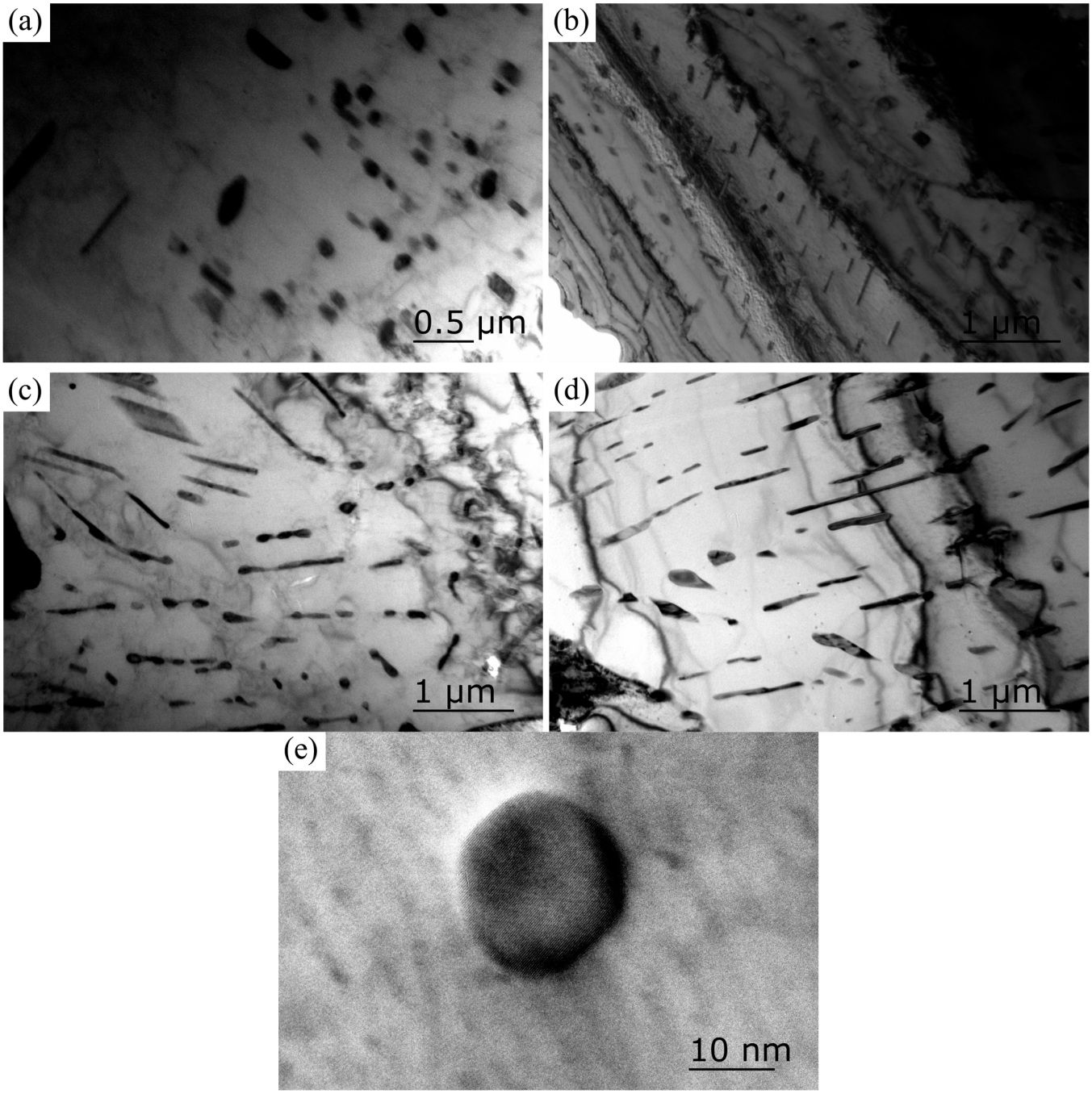


Figure 9. TEM results of gear blank steel: (**a**) air-cooled inner ring; (**b**) air-cooled outer ring; (**c**) forced-air-cooled inner ring; (**d**) forced-air-cooled outer ring; (**e**) partial view of forced-air-cooled outer ring.

As can be seen from Figure 9, under the air cooling process, the gear blank inner and outer ring carbides are mostly elliptical or short bars, with a larger size, which is due to the slower cooling speed, the atomic diffusion is sufficient, the carbide growth time is reorganized, and it is easy to form coarse second-phase particles. Inside the forced-air-cooled process, the outer ring carbides were transformed into short rods or needles with a relatively uniform distribution, and spherical carbide particles with a size of about 10 nm only appeared in the forced-air-cooled outer ring samples. It is due to the faster cooling rate inhibiting the atomic diffusion; carbide nucleation occurs but growth is limited, and ultimately a fine diffuse shape is formed. Comparison of the effect of the location of the regions on the results in Figure 9 reveals the following characteristics in both air

and forced-air cooling: the carbide distribution in the inner ring region is more random, whereas the carbides in the outer ring region are more regularly arranged and uniform in size. This indicates that the outer ring region maintains the characteristics of higher phase transition consistency and more uniform cooling in all the different cooling processes. To further illustrate the composition of the carbide phase, compositional scans were performed on the experimental samples in Figure 9 and the results are shown in Figure 10.

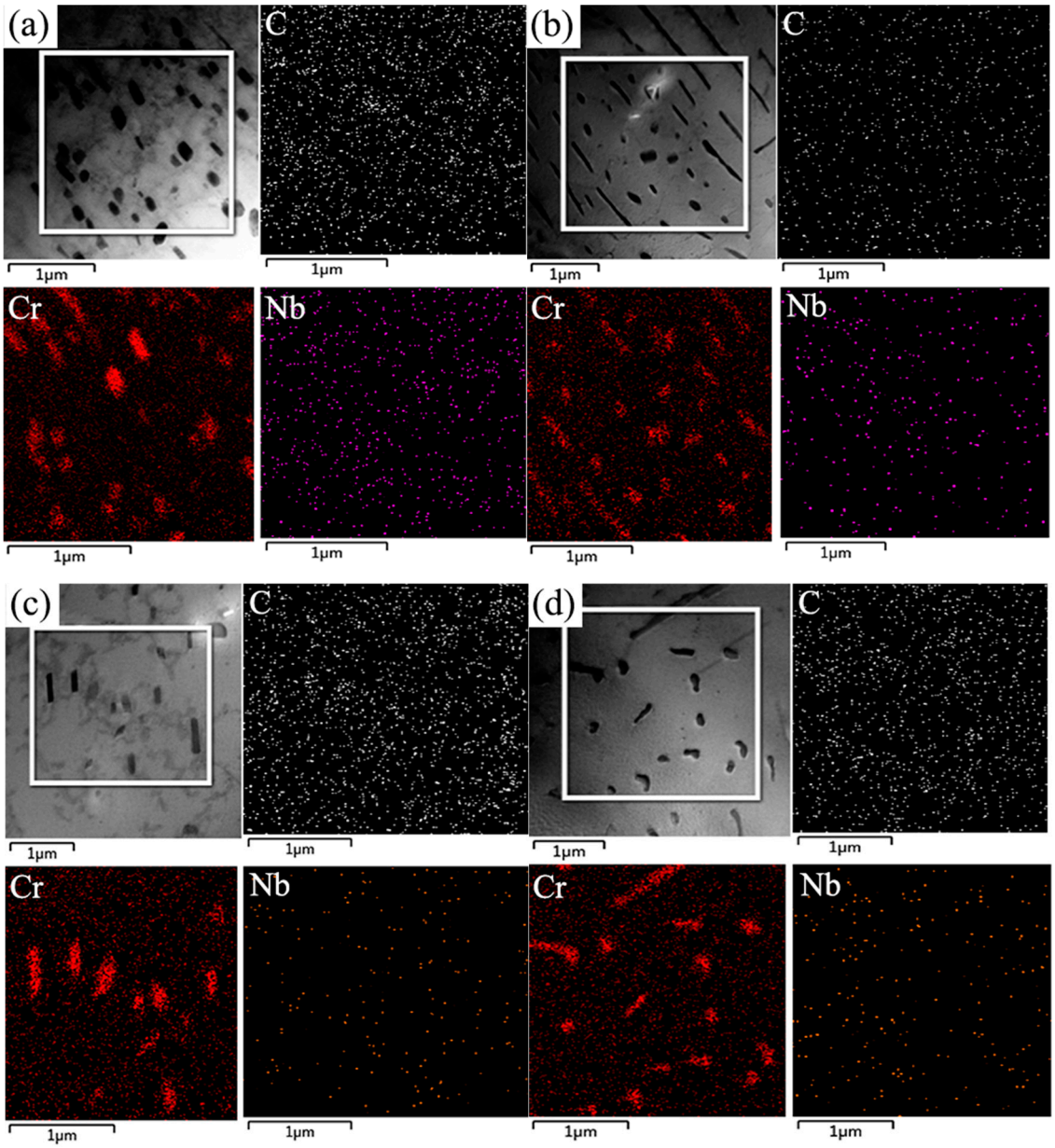


Figure 10. TEM element mapping results of gear blank steel: (**a**) air-cooled inner ring; (**b**) air-cooled outer ring; (**c**) forced-air-cooled inner ring; (**d**) forced-air-cooled outer ring.

From Figure 10, the morphology of the precipitated phase is closely related to the degree of enrichment of Cr. For Nb, although the distribution density is different, the dispersion degree is similar, and none of them form an aggregated distribution, so it can be judged that the Cr-rich carbide is the most important component in the precipitated phase, and the carbide phase composed of Cr_7C_3 determines the size and morphology of the precipitated phase.

Under the condition of low cooling rate, the supercooling degree of the system is small, and the driving force of the phase transition is at a low level, which is in line with the kinetic characteristics of "nucleation-growth" in solid-state phase transition. At this point, the solute atoms have sufficient long-range diffusion capacity, resulting in the nucleated precipitation phase being able to grow rapidly by continuously trapping surrounding solute atoms. It can also be further roughened by the Ostwald ripening mechanism [32,33]; small precipitates dissolve and large precipitates grow to reduce the total interfacial energy of the system, and eventually form coarse and unevenly distributed precipitation tissues. After the cooling rate is increased, the subcooling degree of the system increases significantly, so that the critical nucleation work of the phase transition is greatly reduced, at which time the diffusion is strongly inhibited, the solute atoms can only carry out short-range migration, and the growth process of the precipitated phase is significantly limited. In addition, the stability of the oversaturated solid solution is improved [34], avoiding the full growth of the equilibrium phase and making it easier to form a diffuse distribution of the substable overphase, which ultimately results in a homogeneous distribution of the precipitates.

The slower cooling rate gives the carbide enough time to complete the balanced growth in the three-dimensional direction [35], and eventually forms a spatially more complete block structure. From the energy balance point of view, the precipitated phase-interface is dominated by a non-congruent interface at low cooling rate, the interfacial energy dominates the total energy of the system, and the surface area/volume ratio of the massive precipitates is the smallest under the same volume, so the carbide shows a massive increase. This in turn affects the properties of the surface. Upon increasing the cooling rate, the high nucleation rate intensifies the solute competition between a large number of nuclei, inhibiting the lateral coarsening of individual precipitated phases, which ultimately take on the form of short rods or needles in the form of bars. At the energy balance level, the interface between the high-cooling-velocity precipitation phase and the matrix turns into a semiconformal interface, and the strain energy replaces the interfacial energy as the dominant factor in the system energy. According to the principle of minimizing strain energy [36,37], the lattice distortion accumulation of the bar precipitates is much lower than that of the block for the same volume, and the long axis grows in the direction of low strain in the substrate, which stabilizes the system by reducing the elastic strain energy brought by the mismatch of the crystal surfaces.

3.3. Mechanism Analysis of Cooling Rate Affecting Surface Roughness

3.3.1. Thermodynamic Computational Analysis

To clarify the phase composition and transformation paths under equilibrium conditions and establish a theoretical basis for the microstructure–performance relationship, thermodynamic calculations of the equilibrium transformation characteristics of the gear steel were performed, and the results are shown in Figure 11, in which Figure 11a is the complete full map of the equilibrium transformation characteristics, and Figure 11b is the local zoom-in map of the key transformation intervals. From the calculation results, the steel for gear blank shows a multi-phase continuous phase evolution from the liquid phase by equilibrium cooling to 620 °C, which precipitates δ-phase, γ-phase, Nb (C, N) phase, $M_{23}C_6$ phase, α-phase, and M_7C_3-phase, in order. The formation of each phase corresponds to a specific type of phase transition. The initial stage is the formation of δ phase from the liquid phase through homogenization. With the decrease in temperature, the transformation from δ phase to γ phase is completed through peritectic transformation. After entering the middle temperature range, the Nb (C, N) phase is first formed from the γ phase by desorption and precipitation, and then the $M_{23}C_6$ phase is precipitated again by the desorption and precipitation transformation. When the temperature drops near the

eutectoid point, the γ phase undergoes eutectoid transformation and decomposes into the α phase (ferrite). Final cooling to about 620 °C further precipitates the M_7C_3 phase from the α-phase by a desolvation precipitation transition. Combined with the chemical composition analysis of the steel, both the $M_{23}C_6$ phase and the M_7C_3 phase are chromium-rich carbides, which are directly related to the chromium enrichment and diffusion behavior of the steel.

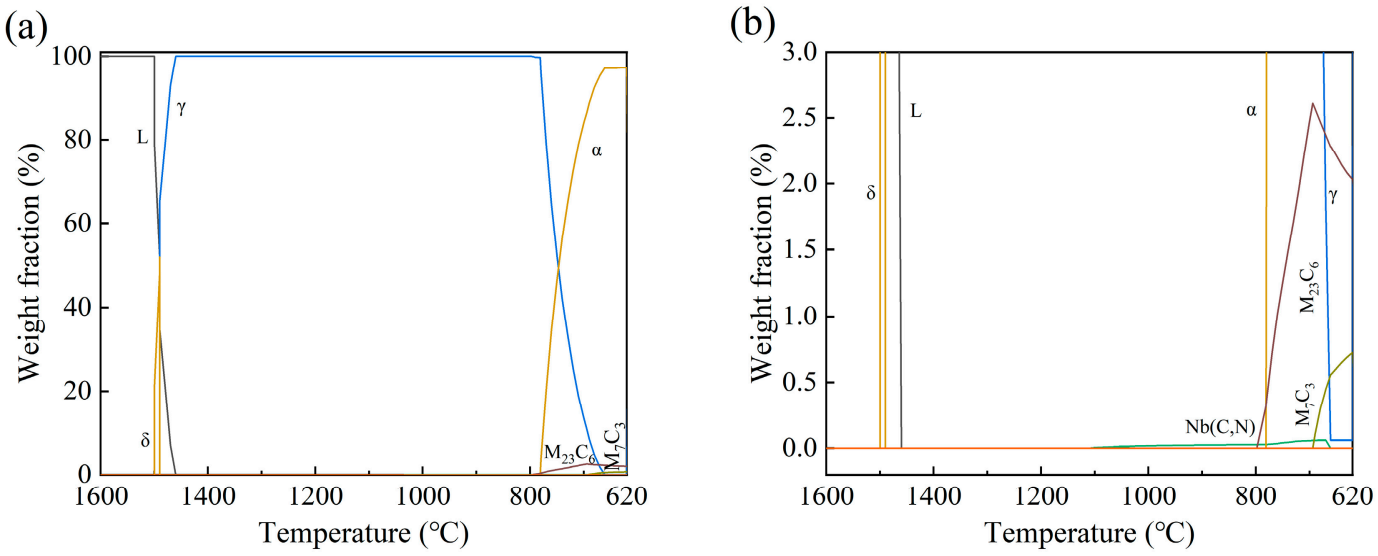


Figure 11. Thermodynamic calculation results of equilibrium transformation for gear steel: (**a**) full diagram; (**b**) partial diagram.

According to the analysis results of Figure 11b, the precipitation behavior of chromium-rich carbide already exists in the system before the eutectoid transformation occurs. According to the thermodynamic characteristics of phase transformation, the $M_{23}C_6$ phase is a stable chromium-rich carbide phase of the steel under equilibrium conditions. In the process of non-equilibrium cooling, due to the limited kinetic conditions of atomic diffusion, chromium-rich carbides exist in the form of metastable M_7C_3 phase. The cooling process from 950 °C to 690 °C belongs to typical non-equilibrium cooling, so the chromium-rich carbide precipitated before eutectoid transformation can be identified as M_7C_3 phase. This conclusion is completely consistent with EBSD phase analysis results, which further verifies the reliability of phase-relative composition determination.

In addition, during the non-equilibrium cooling process, the cooling rate has a significant regulatory effect on the precipitation behavior of chromium-rich carbides; the increase in cooling rate will increase the atomic diffusion resistance, thus hindering or even inhibiting the nucleation and growth of chromium-rich carbides. This trend was confirmed by the differences in semi-quantitative carbide contents in different regions of the gear blanks. During the cooling of air-cooled gear blank outer rings from 950 °C to 690 °C, the cooling rate was relatively fast, and the semi-quantitative content of Cr-rich carbides was lower. However, the cooling rate of the inner ring is relatively slow, and the relative semi-quantitative contents of chromium-rich carbides significantly increases. The difference in semi-quantitative contents between the two is completely consistent with the regulation law of the cooling rate on the precipitation of carbides. Based on the macroscopic and microscopic analysis of carbide precipitation during isothermal normalizing, the possible causes of surface quality defects can be fully described by the schematic diagram in Figure 12.

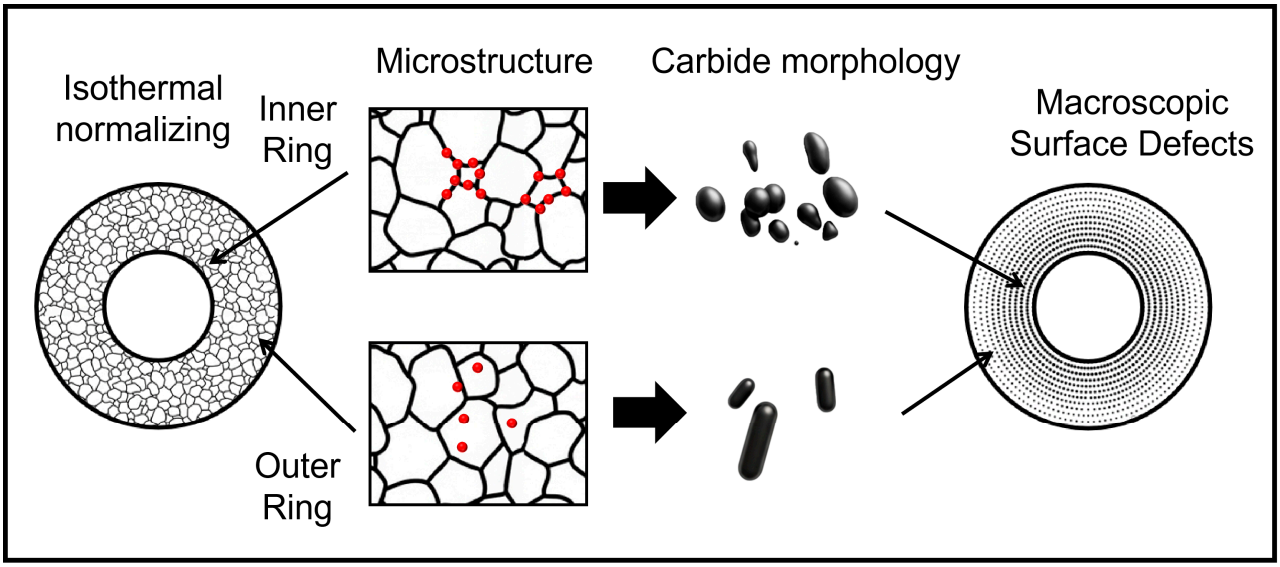


Figure 12. Schematic diagram of the process of surface quality defects in isothermal normalized gear steel.

3.3.2. Differential Scanning Calorimetry (DSC) Analysis

In order to explain the precipitation characteristics of chromium-rich carbides before eutectoid transformation and the inhibition effect of cooling rate increase on precipitation, TG/DSC technology was used to study the phase transformation behavior of gear blank steel during cooling from a high-temperature austenite state to 600 °C at different cooling rates. The results are shown in Figure 13. When the steel for the gear blank was cooled from 1200 °C (fully austenitized temperature) to 600 °C at a cooling rate of 5 °C/min and 20 °C/min, respectively, there were significant sudden heat peaks in the temperature range of 900 °C–800 °C. This thermal signal change is a direct indication of phase transition occurring in the material, and the temperature range is earlier than that of eutectoid transition, indicating that phase transition has occurred in the system before eutectoid transition starts. Combined with the thermodynamic calculation (Figure 11) and the analysis results, it can be concluded that the precipitation process of the phase transformation into Cr-rich carbides occurs in the temperature range of 900 °C–800 °C. However, under the non-equilibrium cooling condition (5 °C/min and 20 °C/min both deviate from equilibrium cooling rate), Cr-rich carbide cannot easily form equilibrium $M_{23}C_6$ phase according to the law of phase transformation kinetics, and its main precipitation form is metastable M_7C_3. By comparing the cooling rates of 5 °C/min and 20 °C/min, it is found that the higher the cooling rate, the higher the precipitation temperature. This is due to the fact that when the cooling rate is low, although the atomic diffusion rate is fast at high temperatures, the degree of carbon supersaturation is low, with the slow decline in temperature carbon saturation gradually increasing. At this time the thermodynamic driving force is enough to overcome the diffusion resistance to be able to form carbides, so the precipitation temperature is low under slow cooling. When cooling is extremely fast, the effective time for atomic diffusion is compressed and carbon atoms are unable to maintain their ability to diffuse while receiving a strong thermodynamic drive (i.e., high supersaturation); therefore, in the high-temperature stage, although the carbon supersaturation is low, the thermodynamic driving force is insufficient and must also be completed before the disappearance of the diffusion capacity. As a result, the carbon atoms need to rapidly reach the critical temperature of atomic diffusion before the "early precipitation", so that the carbides formed at higher temperatures appear.

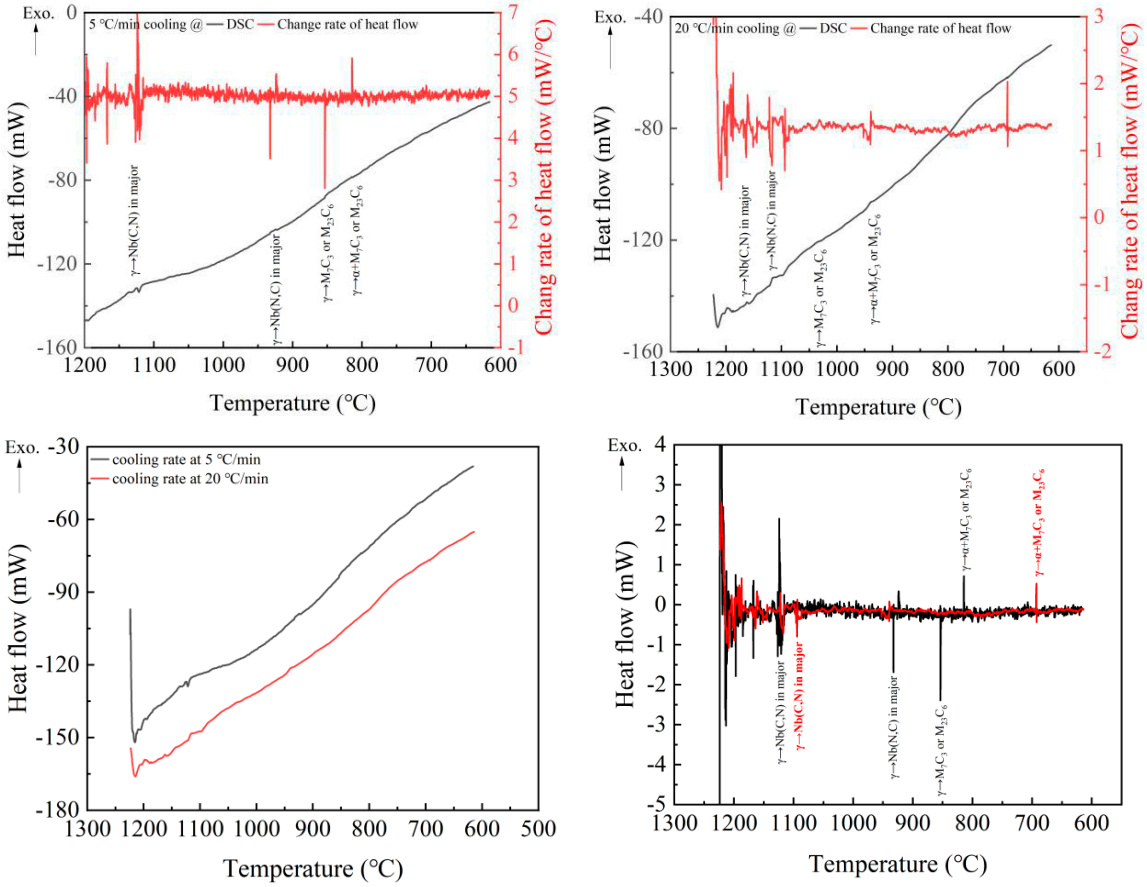


Figure 13. DSC results of gear blank steel.

From the analysis of Figure 13, it can be seen that when the steel for the gear blank is cooled at a low cooling rate during the cooling process, the carbon waits for kinetic conditions while maintaining a high thermodynamic driving force, which delays the carbide precipitation time, resulting in a small or possible overlap interval (around 800 °C) between the difference between the ferrite transformation temperature and the carbide precipitation temperature. Combined with the analysis of EBSD phase distribution results, it is further verified that the chromium-rich carbides will be enriched and precipitated at ferrite grain boundaries at low cooling speeds, thus exacerbating the uneven hardness distribution of the material on the macroscopic and microscopic scales, leading to mechanically polished surface quality defects.

Carbide precipitation in the high-temperature range, when the free energy of precipitation of Cr-rich carbides is lower than the free energy of the austenite matrix, is necessary to meet the thermodynamic conditions for the phase transition to occur spontaneously. At the same time, the austenite matrix did not undergo significant decomposition, providing a stable mother-phase environment for the nucleation and growth of carbides [38,39]. At low cooling rates, carbon slowly accumulates supersaturation in austenite with decreasing temperature, but the thermodynamic driving force is insufficient to reach the precipitation critical value; when the temperature drops to about 800 °C, the thermodynamic driving force is sufficient to overcome the diffusion resistance and initiate carbide precipitation, but this temperature is still in the high-temperature category, centered on the need to complete the aggregation of solute atoms prior to austenite decomposition. At high cooling velocities, the temperature drop rate is fast and the effective window period for atomic diffusion is sharply compressed. If waiting for the carbon supersaturation to accumulate to the critical value, the atomic diffusion ability has been significantly weakened with the

temperature drop, and the solute atoms cannot complete the short-range migration and aggregation, the nucleation process will be hindered, so the precipitation is initiated early at higher temperatures (about 900 °C), and nucleation is accomplished with the help of a short diffusion window at high temperatures, avoiding the risk of not being able to precipitate as a result of low-temperature diffusion obstruction, and ultimately characterized by early precipitation at high temperatures.

The temperature drop is gentle at low cooling rate. Austenite easily precipitates ferrite at grain boundaries first, and grain boundaries as a high-energy defect region can significantly reduce carbide nucleation work. Carbide precipitation occurs slightly later than the ferrite transition at low cooling rates and is enriched at grain boundaries, resulting in the eventual formation of aggregated massive carbides. At high cooling rates, on the one hand, the rapid transformation of austenite to ferrite is inhibited and the nucleation sites at grain boundaries are reduced. On the other hand, the thermal stress induced by rapid cooling induces dislocation proliferation in the collective, causing intracrystalline defects to become dispersed nucleation sites. The result is a uniform distribution of carbides without significant aggregation, which is significantly different from the centralized nucleation at grain boundaries at low cooling speeds.

4. Conclusions

In this study, the effect of isothermal normalization cooling rate on the quality defects of the mechanically polished surface was studied by taking 18CrNiMo7-6 wind power gear blanks as the object, through the study of microstructure and carbide precipitation behavior, and the formation mechanism and process control path of mechanically polished surface roughness and bright spot surface defects were clarified. A limitation of this study is a lack of direct machining experimental evidence, such as cutting force, tool wear and subsurface deformation measurements. The relationship between carbides, hardness and surface quality is considered a potential correlation rather than a confirmed causal mechanism. And the main conclusions are as follows:

1. The cooling rate is the core factor influencing the surface roughness of the 18CrNiMo7-6 gear blank after isothermal normalizing, and it plays a role by regulating the precipitation behavior of Cr-rich carbides. Slow cooling (air cooling, AC) promoted the nucleation and growth of Cr-rich carbides (mainly Cr_7C_3, with a small relative content of $Cr_{23}C_6$ in the inner ring), which tended to aggregate at grain boundaries to form coarse blocky structures. This phenomenon was strongly correlated with inhomogeneous microhardness of the material and the formation of bright spot defects on the machined surface. Fast cooling (forced-air cooling, FA) inhibits atomic diffusion, reduces the relative amount of carbide precipitation, and makes it present a short rod or needle-like diffuse distribution, which strongly correlates with improved microstructural uniformity and surface flatness, as well as reduced macroscopic surface defects.
2. The radial elemental segregation characteristics of the 18CrNiMo7-6 virgin cast blank are hereditary in the subsequent process, and differences in carbide precipitation uniformity occur in the inner and outer rings under the same process. Under air cooling conditions of the inner ring of the gear blank, due to the lower cooling rate, C, Cr elemental segregation is more significant, and the increasing trend of surface quality defects during the inner ring cutting process may be related to this.
3. During non-equilibrium cooling, the Cr-rich carbides mainly exist in the form of sub-stable M_7C_3 phase, which precipitates before the eutectic transition. At low cooling rates, the carbide precipitation temperature is low (about 800 °C), and the carbon atoms have enough time to enrich at the grain boundaries to form coarse

carbides; at high cooling rates, atomic diffusion is limited and carbide nucleation is initiated earlier at higher temperatures (about 900 °C), resulting in the formation of diffusely distributed fine carbides. The conclusions of this study are mainly applicable to 18CrNiMo7-6 steel, and further investigations are required to validate their applicability to other alloyed steels with different segregation tendencies.

Author Contributions: Y.W.: data curation, investigation, writing—original draft. A.D.: conceptualization, data curation, investigation. G.J.: methodology, project administration, resources. S.W.: formal analysis, validation. S.Y.: investigation, validation. Z.H.: conceptualization, writing—review and editing, funding acquisition, supervision. All authors have read and agreed to the published version of the manuscript.

Funding: This research was funded by Anhui Provincial Key Research and Development Program (202304a5020082) and Anhui Province's Major Industrial Innovation Program (AHZDCYCX-LSDT2023-01).

Data Availability Statement: The original contributions presented in this research are included in the article. Further inquiries can be directed to the corresponding author.

Conflicts of Interest: Authors Guozhong Jin and Shengfu Wu are employed by the Technical Center, Maanshan Iron and Steel Co., Ltd. The remaining authors declare that the research was conducted in the absence of any commercial or financial relationships that could be construed as a potential conflict of interest.

References

1. Wang, G.; Sang, X.; Zhang, Y.; Zhao, M.; Xu, G.; Peng, Z. Carburization-induced microstructure evolution and hardening mechanism of 18CrNiMo7-6 steel. *J. Mater. Res. Technol.* **2023**, *25*, 1649–1661. [CrossRef]
2. Burkart, K.; Eisenträger, J. Comprehensive analysis of very high cycle fatigue and crack propagation in 18CrNiMo7-6 gear steel for aerospace applications. *Eng. Fract. Mech.* **2025**, *325*, 111277. [CrossRef]
3. Wu, J.; Wei, P.; Liu, G.; Chen, D.; Zhang, X.; Chen, T.; Liu, H. A comprehensive evaluation of DLC coating on gear bending fatigue, contact fatigue, and scuffing performance. *Wear* **2025**, *536*, 205177. [CrossRef]
4. Fernandez, R.C.; Tobie, T.; Rommel, S.; Collazo, J. Improve wind gears bending performance by means of IGS (Improved gear surface). *Int. J. Fatigue* **2023**, *172*, 107618. [CrossRef]
5. Mandal, P.; Olasolo, M.; Da Silva, L.; Lalvani, H. Impact of a Multi-step Heat Treatment on Different Manufacturing Routes of 18CrNiMo7-6 Steel. *Metall. Mater. Trans. A* **2020**, *51*, 3009–3029. [CrossRef]
6. Yang, S.; Chen, W.; Liang, R. Residual stresses in gear form grinding by considering carburizing heat treatment: Multi-field coupled numerical simulation and experimental verification. *Int. J. Adv. Manuf. Technol.* **2024**, *131*, 4981–4999. [CrossRef]
7. Wang, W.; Liu, H.; Zhu, C.; Du, X.; Tang, J. Effect of the residual stress on contact fatigue of a wind turbine carburized gear with multiaxial fatigue criteria. *Int. J. Mech. Sci.* **2019**, *151*, 263–273. [CrossRef]
8. Zhang, B.; Liu, H.; Bai, H.; Zhu, C.; Wu, W. Ratchetting–multiaxial fatigue damage analysis in gear rolling contact considering tooth surface roughness. *Wear* **2019**, *428–429*, 137–146. [CrossRef]
9. An, X.; Tian, Y.; Wang, H.; Wang, Z. Effect of Preheat Treatment on Microstructure and Properties of a Gear Steel for High-Temperature Carburizing. *Steel Res. Int.* **2020**, *91*, 2000180. [CrossRef]
10. Lee, S.; Ahmadi, Z.; Pegues, J.W.; Mahjouri-Samani, M.; Shamsaei, N. Laser polishing for improving fatigue performance of additive manufactured Ti-6Al-4V parts. *Opt. Laser Technol.* **2021**, *134*, 106639. [CrossRef]
11. Wu, L.; Lv, Y.; Zhang, Y.; Li, A.; Ji, V. Contact Fatigue Behavior Evolution of 18CrNiMo7-6 Gear Steel Based on Surface Integrity. *Metals* **2023**, *13*, 1605. [CrossRef]
12. Zhu, X.; Dong, Z.; Zhang, Y.; Cheng, Z. Fatigue Life Prediction of Machined Specimens with the Consideration of Surface Roughness. *Materials* **2021**, *14*, 5420. [CrossRef]
13. Jiang, W.; Qu, J.-J.; Liu, F.; Yue, G.; Zhou, L.; Luo, Y.-C.; Ning, H.-W. Effect of Scanning Electron Beam Pretreatment on Gas Carburization of 22CrMoH Gear Steel. *Coatings* **2024**, *14*, 611. [CrossRef]
14. Wu, J.; Wei, P.; Liu, H.; Zhang, X.; He, Z.; Deng, G. Evaluation of pre-shot peening on improvement of carburizing heat treatment of AISI 9310 gear steel. *J. Mater. Res. Technol.* **2022**, *18*, 2784–2796. [CrossRef]
15. Tang, L.; Jia, W.; Hu, J. An enhanced rapid plasma nitriding by laser shock peening. *Mater. Lett.* **2018**, *231*, 91–93. [CrossRef]

16. Lamim, T.S.; Bernardelli, E.A.; Bendo, T.; Mello, C.H.; Binder, C.; Klein, A.N. Duplex surface treatment of sintered iron by plasma nitriding and plasma carburizing at low temperature. *Surf. Coat. Technol.* **2019**, *375*, 911–919. [CrossRef]
17. Liu, Z.; Peng, Y.; Chen, C.; Gong, J.; Jiang, Y. Effect of surface nanocrystallization on low-temperature gas carburization for AISI 316L austenitic stainless steel. *J. Mater. Res. Technol.* **2020**, *182*, 104053. [CrossRef]
18. Balusamy, T.; Narayanan, T.S.N.S.; Ravichandran, K.; Park, I.S.; Lee, M.H. Plasma nitriding of AISI 304 stainless steel: Role of surface mechanical attrition treatment. *Mater. Charact.* **2013**, *85*, 38–47. [CrossRef]
19. Dong, Y.; Cui, X.; Li, J.; Hu, Y.; Jin, G.; Li, Q.; Liu, J.; Fan, P. Effect of carburizing nitriding compound treatment on microstructure evolution and properties of low carbon gear steel. *Mater. Chem. Phys.* **2025**, *337*, 130489. [CrossRef]
20. Lv, Y.; Lei, L.; Sun, L. Influence of different combined severe shot peening and laser surface melting treatments on the fatigue performance of 20CrMnTi steel gear. *Mater. Sci. Eng. A* **2016**, *658*, 77–85. [CrossRef]
21. Güngör, S.; Edwards, L. Effect of surface texture on the initiation and propagation of small fatigue cracks in a forged 6082 aluminium alloy. *Mater. Sci. Eng. A* **1993**, *160*, 17–24. [CrossRef]
22. Arola, D.; Williams, C. Estimating the fatigue stress concentration factor of machined surfaces. *Int. J. Fatigue* **2002**, *24*, 923–930. [CrossRef]
23. Chen, J.; Yang, T.; Chen, S.; Jiang, Q.; Li, Y.; Chen, X.; Xu, Z. Multi-Objective process parameter optimization of ultrasonic rolling combining machine learning and Non-Dominated sorting genetic Algorithm-II. *Materials* **2024**, *17*, 2723. [CrossRef]
24. Zhang, Y.; Liu, M.; Han, J.; Zhai, S.; Liu, X.; Yan, X.; Nie, F.; Peng, Z. Hard-turning-induced surface integrity and fatigue performance of 18CrNiMo7-6 steel for V-notched specimens. *Precis. Eng.* **2026**, *97*, 268–278. [CrossRef]
25. Liu, X.; Yu, W.; Che, H.; Zhang, J.; Zhu, J.; Jiang, Q.; Zhang, C.; Wang, M. The Effect of Cyclic Heat Treatment on the Microstructure and Mechanical Properties of 18CrNiMo7-6 Gear Steel. *Materials* **2024**, *17*, 5855. [CrossRef]
26. Mo, J.; Yuan, Q.; Liang, W.; Zhang, Z.; Hu, H.; Xu, G. Effect of the Normalizing Temperature on the Size and Homogeneity of Austenite Grain in 20CrMnTi Carburized Gear Steel. *Arab. J. Sci. Eng.* **2024**, *50*, 13593–13604. [CrossRef]
27. Longbang, W.; Cuili, Z. Analysis and preventive measures for the coarse microstructure of 20CrMoH steel gears after carburizing and quenching. *MW Met. Form.* **2024**, *9*, 74–77,83.
28. Babasafari, Z.; Pan, A.V.; Pahlevani, F.; Hossain, R.; Sahajwalla, V.; Du Toit, M.; Dippenaar, R. Effects of austenizing temperature, cooling rate and isothermal temperature on overall phase transformation characteristics in high carbon steel. *J. Mater. Res. Technol.* **2020**, *9*, 15286–15297. [CrossRef]
29. Hunkel, M.; Kagathara, J.; Prahl, U. The Influence of Segregations after Forming on the Heat Treatment Result of Bevel Gears. *Steel Res. Int.* **2019**, *90*, 1800427. [CrossRef]
30. Xiong, J.; Zhang, H.; Nie, F.; He, F.; Yang, J.; Hu, Z.; Wen, Z.; Zhao, H.; Yuan, X. Formation mechanisms for (Cr, Co) 7C3/(Cr, Co) 23C6 heterogeneous precipitates and stacking faults around carbides in surfacing welding of stellite alloy on stainless steel. *Met. Mater. Int.* **2022**, *28*, 1639–1649. [CrossRef]
31. Cai, X.; Shen, M.; Cao, B.; Liu, M.; Xu, Y. Microstructural characterization of chromium carbide-reinforced iron matrix composites prepared by combination of casting and heat treatment. *Vacuum* **2023**, *216*, 112477. [CrossRef]
32. Dai, Z.; Yang, Z.; Zhang, C.; Chen, H. Incomplete carbon partitioning during quenching and partitioning of Fe–C–Mn–Si steels: Modeling and experimental validations. *Acta Mater.* **2020**, *200*, 597–607. [CrossRef]
33. Zheng, Y.; Chu, S.; Zhang, L.; Wang, Q.; Qiu, G.; Zhu, L.; Guo, Z.; Xie, T.; Zhao, H.; Lu, S. Research on microstructure evolution and carbide transformation behavior during the quenching and tempering processes of secondary hardening steel. *J. Mater. Res. Technol.* **2025**, *33*, 8088–8107. [CrossRef]
34. Xiang, J.; Yang, H.; Zhuang, C. Effect of Cooling Rate on the Characteristics of Eutectic Carbides in M2Al High-Speed Steel. *Crystals* **2025**, *15*, 493. [CrossRef]
35. Wittenzellner, T.; Sumarli, S.; Dai, Z.; Cocen, O.; Schaar, H.; Wang, F.; Ma, D.; Bührig-Polaczek, A. Influence of Process Parameter and Alloy Composition on Misoriented Eutectics in Single-Crystal Nickel-Based Superalloys. *Materials* **2023**, *16*, 4477. [CrossRef]
36. Shin, D.; Poplawsky, J.D.; Chisholm, M.F.; Allard, L.F.; Haynes, J.A.; Shyam, A. The many faces of θ′-Al2Cu precipitates: Energetics of pristine and solute segregated Al/θ′semi-coherent interfaces. *Acta Mater.* **2024**, *281*, 120444. [CrossRef]
37. Liu, D.; Xue, Z.; Song, S. Effect of cooling rate on non-metallic inclusion formation and precipitation and micro-segregation of Mn and Al in Fe–23Mn–10Al–0.7 C steel. *J. Mater. Res. Technol.* **2023**, *24*, 4967–4979. [CrossRef]
38. Jiang, D.; Zhang, L. Influence of cooling parameters on the microstructure and primary carbide precipitation in GCr15 steel. *Steel Res. Int.* **2021**, *92*, 2100208. [CrossRef]
39. Bai, Z.; Zhang, L.; Shu, T.; Wu, X.; Shen, M. Carbide Precipitation Behavior and Impact Toughness of Austenitic Hot-Forging Die Steels after Long-Term Holding at High Temperatures. *Steel Res. Int.* **2025**, *97*, 709–718. [CrossRef]

Disclaimer/Publisher's Note: The statements, opinions and data contained in all publications are solely those of the individual author(s) and contributor(s) and not of MDPI and/or the editor(s). MDPI and/or the editor(s) disclaim responsibility for any injury to people or property resulting from any ideas, methods, instructions or products referred to in the content.